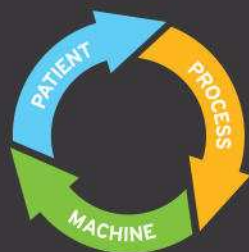


# SunCHECK™ YOUR NEW INTEGRATED PLATFORM FOR QA



PATIENT QA  
MACHINE QA  
DEVICES & DATA  
**ONE WORKFLOW.**



# Spine surface detection from local phase-symmetry enhanced ridges in ultrasound images

Peer Mohamed S. Shajudeen and Raffaella Righetti<sup>a)</sup>

*Department of Electrical and Computer Engineering, Texas A&M University, College Station, TX 77840, USA*

(Received 4 April 2017; revised 29 May 2017; accepted for publication 23 June 2017; published 21 September 2017)

**Purpose:** Improper administration of epidural anesthesia can result in nerve complications. This problem is exacerbated for obese patients whose vertebrae cannot be palpated. Ultrasound (US) has recently emerged as an attractive imaging modality for accurate epidural placement. However, anesthesiologists untrained in US have difficulty interpreting the anatomy in noisy spinal US images. Furthermore, the complex geometry in spinal US images is characterized by a discontinuous intensity profile because the transducer is often not perpendicularly oriented to spine surface regions such as laminae, articular and transverse processes. This makes the interpretation of spinal images more challenging than typical long bone surface images. In this article, we propose a new method to segment the spine anatomy in US images obtained in both the transverse and paramedian planes.

**Methods:** A set of 108 B-mode images were randomly chosen from 35 cine loops obtained from scanning the lumbar and thoracic vertebrae of 17 healthy volunteers with a BMI ranging from 19.5 to 27.9. A local phase-symmetry technique was applied to the B-mode images for enhancement of bone-like ridges, and the spine blobs were subsequently classified. The segmented spine surface from the blobs was compared against a radiologist's manual delineation of the spine surface.

**Results:** For the performance of the spine blob classifier, we obtain a Matthews Correlation Coefficient (MCC) of 0.77 and a geometric mean (G-mean) of 0.96. The mean absolute error between the manual delineation of the laminae by the radiologist and the automatic laminae segmentation is found to be 0.26 mm with a maximum possible absolute error of 2.01 mm for spinal US images of 70 mm depth.

**Conclusions:** Our proposed technique successfully performs automatic segmentation of the spine surface — specifically the laminae, ligamentum flava, spinous, transverse, and articular processes — and can be extended to any bone anatomy present in an US image. This has implications for 3D visualization of bone surfaces and, without loss of generality, the vertebral column. © 2017 American Association of Physicists in Medicine [<https://doi.org/10.1002/mp.12509>]

Key words: bone enhancement, bone segmentation, epidural, phase symmetry, spine, ultrasound

## 1. INTRODUCTION

Spinal ultrasound (US) has known to offer many potential benefits for intra-operative surgery scenarios. This can be attributed to some of the distinctive qualities of US such as portability, safety, and cost effectiveness. US has been used as a screening tool for administering spinal injections.<sup>1</sup> Epidural anesthesia is performed in 75% of all childbirths in the United States with a 70% failure rate among obese patients.<sup>2</sup> Regional anesthesia for placement of the epidural needle relies on palpation of anatomical landmarks, but the optimal puncture depth cannot be determined from inspection or palpation especially for obese patients. This can result in patient discomfort, accidental dural puncture, and potential trauma to the nerves, vessels, bones, and ligaments.<sup>3</sup> Multiple insertion attempts could result in nerve damage causing epidural abscess infection.<sup>4</sup> Other complications of neuraxial anesthesia involve spinal hematomas, bleeding diathesis, and left ventricular outflow obstruction. X-ray-based fluoroscopy is the only competing real-time intra-operative modality with US,<sup>5</sup> but it is not portable and uses ionizing radiations.

US has been successfully used in addressing the need for accurate epidural placement.<sup>2,3,6,7</sup> However, the learning curve for anesthesiologists has not been established to fruition.<sup>8</sup> There are two approaches to performing spinal US scans. Scanning along the transverse plane involves placing the US probe perpendicular to the long axis of the vertebral column, and the paramedian plane involves placing the US probe parallel to the long axis of the vertebral column while tilted at an angle. The anesthesiologist/operator would first identify the appropriate interspace level using the paramedian approach and then place the transducer along the transverse plane when administering the epidural or spinal. Most of the existing literature has focused on using the paramedian approach for identifying lumbar interspace levels.<sup>6,7,9,10</sup> However, the transverse plane approach, which is predominantly used for the US images shown in this article, has been found to be the preferred method for accurate estimation of the insertion point.<sup>11</sup> This is due to easier identification of the depth from the skin to the ligamentum flavum. Despite its potential advantages, US has not yet become the standard-of-care for epidural placement due to the difficulty in interpreting spinal anatomy by anesthesiologists untrained in US.<sup>12</sup>

Spine surface detection in US images requires a robust bone segmentation technique that reduces the influence of the soft-tissue interface and ultrasonic imaging artifacts (reverberation, speckle, etc.). A bone feature is a hyperechoic line profile with a perceivable level of posterior acoustic shadowing (black region) underneath the feature. Figure 1 shows an ideal segmentation of the lumbar spine (bone feature) for an US image obtained using the transverse plane approach. This level of continuity in the spine line profile is rarely possible. The intensity along the ideal line profile between the laminae and the spinous process is not sufficiently pronounced, which leads to a large discontinuity in the automatically segmented image.

US bone segmentation has been extensively investigated in the past. US images of bones usually feature nonuniform intensity due to scattering between bone–tissue interfaces. Therefore, simple intensity-based thresholding methods are, in general, inadequate for US bone segmentation. Some groups have employed intensity information and gradient-based operators for the segmentation.<sup>13–15</sup> However, these methods are sensitized to machine setting parameters (operating frequency, gain, and acoustic power), which affect the image contrast and resolution. US artifacts and high curvature bone anatomy also affect the hyperechogenicity of the bone surface. For example, Kowal et al.<sup>14</sup> proposed a fast automated bone contour detection algorithm where a higher intensity weighting is applied for deeper structures. While the method may be suitable for deep bony regions that may have nonuniform intensities, the merging of large area connected components may not work for bone fractures or a discontinuous spine line profile. To address this limitation, *a priori* knowledge about the bone appearance has been incorporated into the bone contour modeling criteria,<sup>16–19</sup> but this can be limiting when applied to the complex geometry of a spine especially in the transverse view. Due to the large discontinuities in the hyperechogenicity of the spine line profile, especially between the laminae and the spinous processes, evolving a contour can result in it veering out of the spine boundary constraints. Active contour techniques are also susceptible to contrast and intensity variations due to the

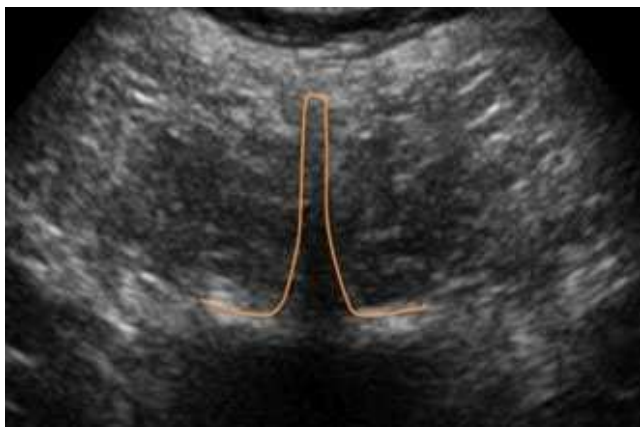


FIG. 1. Actual lumbar spine region delineated on a US image obtained in the transverse plane. [Color figure can be viewed at [wileyonlinelibrary.com](http://wileyonlinelibrary.com)]

intensity gradient influence on the external energy term in the models.

Elastography has been suggested as a potential aid to ultrasonography for bone surface localization due to the high mechanical contrast between bones and surrounding soft tissue,<sup>20–22</sup> but it has not been investigated for spinal applications yet. Strain patterns in proximity of spines may be affected by the complexity of the spine geometry as well as adjoining soft tissues, erector spinae muscles and ligaments conjoined with the laminae, and transverse and articular processes that lie deeper down the skin surface.

Local phase-based localization of the bone surface has gained a lot of traction in recent years due to its robustness from using intensity invariant measures. Hacıhaliloglu et al.<sup>23</sup> and Hacıhaliloglu et al.<sup>24</sup> used a Log-Gabor filter based phase-symmetry measure to produce a strong response on the bone surface. The automated parameter estimation technique for Log-Gabor filters attempts to suppress nonbone responses elsewhere in the B-mode image but is prone to false-positive bone responses at soft-tissue interfaces that have similar intensity profiles as the bone surface.<sup>22–24</sup>

Little attention has been paid to spine surface segmentation in US images especially those obtained in the transverse plane. Khallaghi et al.,<sup>25</sup> Behnami et al.,<sup>26</sup> Rasoulzadeh et al.,<sup>27</sup> and Nagpal et al.<sup>28</sup> have incorporated statistical shape, pose, and scale priors obtained from segmented vertebral CT slices co-registered with spinal US images. Since the spinal US images have no prior enhancement, the quality of the vertebral features used for registration depends on the intensity profile of the spine surface. Hacıhaliloglu et al.<sup>29</sup> overcame this limitation by using phase-based localization as applied to spine surfaces. Despite the promising results of laminae enhancement, the influence of soft tissue was still evident. In some cases, this was reduced by the addition of bottom-up ray casting, which could fail in the presence of nonzero intensities following the bone surface. Tran and Rohling<sup>6</sup> have proposed the use of a lamina template to detect laminae obtained using phase-based localization. Both techniques<sup>6,29</sup> are restricted to work for paramedian plane images. Yu et al.<sup>30</sup> proposed a template-based technique to detect the epidural space in transverse plane images, but this technique may be sensitive to contrast and gain parameters set in the machine. In addition, template-driven techniques<sup>6,30</sup> are restricted to work for lumbar anatomy and are not scalable to structural changes in the vertebra. Berton et al.<sup>31</sup> developed a spine detection algorithm for the transverse plane deriving features like phase symmetry, rupture points for shadowing, and texture descriptors to classify the spinous process and acoustic shadow. This technique is restricted to detecting the spinous process region, which is beneficial for scoliosis measurement. The authors did not demonstrate a procedure for extracting other anatomical structures characteristic of the vertebrae such as the laminae.

In this article, we propose a fully automatic spine surface segmentation technique that detects spine surface regions such as spinous processes, articular processes, transverse processes, laminae, and also dense fibrous tissue like the



ligamenta flava-dura mater interface (LF) for US images obtained in both the transverse plane and paramedian plane. The novelty of our method lies in the feature development for the design of our classifier that detects the spine surface regions. Potential applications of our technique include the following:

- Superimposing the detected spine surface line profile on the B-mode image in the transverse plane enables easy visualization of the skin to LF distance/puncture depth facilitating accurate epidural placement.
- The 2D images postspine surface detection along with position coordinates information can be stacked together to perform 3D volume reconstruction of the vertebral column.

## 2. METHODS

### 2.A. Speckle reduction using a first-order statistics filter

Degradation of US images can rise from speckle, which can be modeled as locally correlated multiplicative noise. Speckle is caused by the constructive and destructive interference between US waves scattered from tissues. A linear filter using first-order statistics such as local mean and variance from sliding window operations has been proposed for speckle reduction in Ref. [32]:

$$f(x, y) = \bar{I}_n + \left[ \frac{\sigma_n^2 - \sigma^2}{\sigma_n^2} \right] (I(x, y) - \bar{I}_n) \quad (1)$$

where  $f(x, y)$  is the speckle-reduced pixel,  $I(x, y)$  is the pixel intensity from the original US image, and  $\sigma^2$  is the variance of the original US image. Local statistics such as mean and variance of the  $3 \times 3$  pixel neighborhood of  $I(x, y)$  are given by  $\bar{I}_n$  and  $\sigma_n^2$ , respectively. The speckle-reduced image [an example is shown in Fig. 2(b)] is normalized between 0 and 1 to enhance the contrast of the image. The speckle-reduced image is the input to the ridge enhancement and classification steps of the algorithm and will be termed as the “US image” in the remaining of the article.

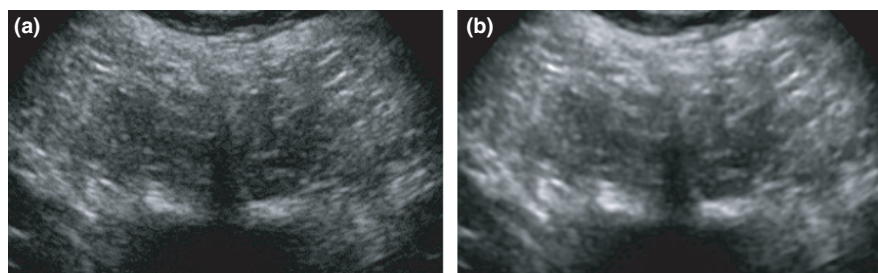


FIG. 2. (a) Original 2D US image of a human subject's lumbar vertebra *in vivo*. (b) The image after the application of a first-order statistics filter on Fig. 2(a).

### 2.B. Local phase-symmetry-based ridge enhancement (PSRE) in spinal US images

Our proposed phase-symmetry ridge enhancement (PSRE) algorithm can be applied to surface localization of any type of bones in addition to spine. Therefore, we will use the terms “bone” and “spine” interchangeably in this section. Bone surfaces in US images are generally described by a continuous bright region. In Fig. 3, we show an elevation map of an US image depicting a cross-sectional view of a spine with intensity of the image along the elevational direction in the map. The elevation map is analogous to a mountain range. Edges are double-line patterns representing the upward and downward slopes of each mountain. Their strength is proportional to the steepness of the slope of a mountain. Ridges, which capture highly specular surfaces including bone surfaces, have maximal strength at the medial axis on each mountain.

In our algorithm, bone surface localization is performed using phase symmetry, and it is inspired by studies presented in Refs. [23,24,33]. Phase symmetry is a contrast and illumination invariant ridge detection technique.<sup>34</sup> A Log-Gabor filter bank is used to construct the phase-symmetry model. The broad bandwidth of Log-Gabor filters provides maximal spectral coverage, and the zero DC value ensures maximal spatial localization. Due to the absence of a DC component, Log-Gabor filters have to be constructed in the frequency domain. In the frequency domain, these filters are formed by the product of the Gaussian radial component that responds

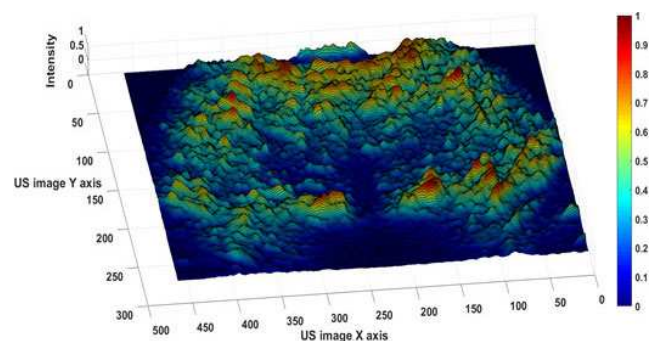


FIG. 3. An elevation map of an US image in which the high peaks and ridges mark the high-intensity regions corresponding to spine-like surfaces. [Color figure can be viewed at [wileyonlinelibrary.com](http://wileyonlinelibrary.com)].

to the filter's spectral bandwidth and the angular component that responds to the filter's orientation, i.e.,

$$G(\omega, \phi) = \exp \left[ - \left( \frac{\ln \left| \frac{\omega}{\omega_0} \right|^2}{\ln \left| \frac{\kappa}{\omega_0} \right|^2} \right)^2 \right] \times \exp \left[ - \left( \frac{(\phi - \phi_0)^2}{2\sigma_\phi^2} \right) \right] \quad (2)$$

where  $\omega_0$  is the filter's center frequency given by the reciprocal of the filter scale or  $1/s$  and  $\phi_0$  is the orientation of the filter. In our study, we empirically set the Gaussian angular bandwidth  $\sigma_\phi = 50^\circ$ . The ratio  $\kappa/\omega_0 = 0.33$  is obtained as a function of the speckle size's full width half maximum (FWHM) as described in Ref. [24].

The local phase of an image is obtained by convolving the US image with the even response and the odd response of the Log-Gabor filter.<sup>23</sup> In the frequency domain, this convolution becomes a multiplication, and it is given in Eq. (3), with  $\mathcal{F}$  denoting the respective Fourier transforms:

$$L(x, y) = \mathcal{F}^{-1} \{ \mathcal{F} \{ f(x, y) \} \cdot G(\omega, \phi) \} \quad (3)$$

The 2D phase-symmetry measure is the difference between the even filter and odd filter responses denoted by the real part and imaginary part of the Log-Gabor filter response, respectively. When a feature with medial axis symmetry is encountered, the difference between the even and odd filter responses is relatively large resulting in the detection of a ridge in the image. This difference is defined in Eq. (4) summed over  $N_s = 3$  scales, and  $N_\phi = 3$  orientations and is sufficient to enhance a smooth, continuous spine ridge.

$$PS(x, y) = \sum_{N_\phi} \sum_{N_s} \frac{|Re\{L(x, y)\}| - |Im\{L(x, y)\}| - T}{\sqrt{(Re\{L(x, y)\})^2 + (Im\{L(x, y)\})^2} + \epsilon} \quad (4)$$

Here,  $\epsilon$  is a small number that prevents division by zero and  $T$  is the shrinkage noise threshold calculated from the smallest scale filter response.  $T$  is computed to be three standard deviations from the mean of the Rayleigh distributed noise.<sup>30</sup> Inadequate selection of the scale  $s$  and orientation  $\phi_0$  parameters could result in amplification of speckle noise, artifact enhancement or significant blurring of the bone feature in the US images. The

algorithm for the automatic selection of these parameters proposed in Refs. [24,33] is employed. The three initial filter orientations are obtained from the Radon transform of the US image by clustering its highest means. The mean of the orientations in the fifth class and two standard deviations from it are used as initial orientations. These orientations are used in generating a ridge strength measure  $A_\gamma$  formed by the  $\gamma$ -normalized eigenvalue difference of the  $L(x, y)$  Hessian. The sum of all pixels is computed for each ridge strength image generated from scale values ranging from  $s = 10$  pixels through  $s = 100$  pixels. The scale value corresponding to the maximum sum is used as the optimal filter scale and is shown in Eq. (5).

$$s^{(i)} = \operatorname{argmax}_s \sum_{x,y} A_\gamma(s, x, y) \quad (5)$$

The Radon transform  $R_\phi$  of the ridge strength image is computed for each scale such that the orientation corresponding to the maximum value of  $R_\phi$  is extracted as shown below:

$$\phi_0^{(i)} = \operatorname{argmax}_\phi R_\phi[A_\gamma(s^{(i)}, x, y)] \quad (6)$$

The above Log-Gabor filter parameters are used in Eq. (4) for obtaining the PSRE image [Fig. 4(a)]. The PSRE image is then binarized for morphological processing [Fig. 4(b)].

## 2.C. Feature space design for spine blob classification

For the remaining of the article, we will be using the term “blobs” for ridge features. The blobs can represent spine but also soft tissue that is not bone or specular artifacts. We observe that the spinous process blobs appear to be the smallest sized blobs in the US images. A simple morphological opening operation eliminating connected components below 50 pixels is used to eliminate small blobs that can be typified as specular artifacts or the influence of scatterers. The connected component threshold of 50 pixels was chosen based on the following observation. A set of 60 spinous process blobs were randomly chosen from vertebral US images and the lowest areas were found to be roughly 100 pixels. The connected component threshold is conservatively set to be half the minimum value. From the remaining foreground pixels, which serve as the binarized PSRE image shown in

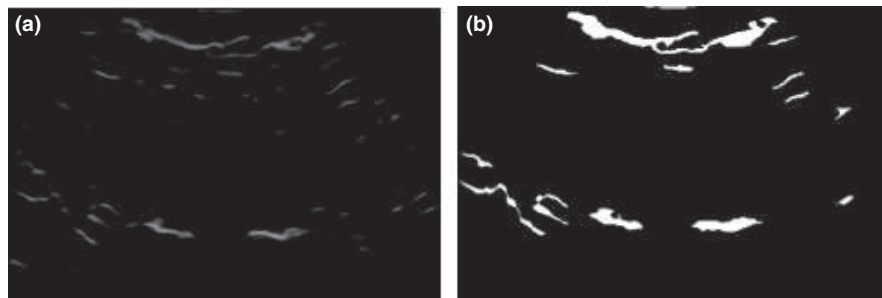


FIG. 4. (a) Ridge enhanced image using phase symmetry (PSRE image). (b) The binarized PSRE image after morphological area opening with 14 blobs retained.

Fig. 4(b), we will be extracting features for classifying these pixels into spine or nonspine blobs. The nonspine blobs are the ones corresponding to soft tissue or artifacts. We will be using two features to perform the spine surface detection of the blobs: (a) Mean pixel intensity and (b) Sum of squared residuals of the shadow region row means signal as detailed in the following.

### 2.C.1. Mean pixel intensity

The mean intensity of each blob can be obtained by multiplying the binarized PSRE image with the US image and calculating the mean of pixel intensities of each blob. Since the nonspine blob regions could result in an equal or higher mean value of the spine blob regions, a spinal region-enhanced US image is necessitated. The enhancement should lead to a higher weighting for the shadow region and the blobs immediately above it. A shadow function inspired by studies in Ref. [16] is first used in which each intensity value in the US image is taken to be the average cumulative sum of the previous intensity values in each scanline. We then take the image complement of the normalized shadow function and square it to get the Acoustic Shadowing Energy (ASE) [Eq. (7)]. The  $Norm_{[0,1]}$  operator indicates normalization of image intensities between 0 and 1.

$$ASE(x, y) = \left( 1 - Norm_{[0,1]} \left\{ \frac{1}{\# \text{ of rows}} \sum_{i=x}^{\# \text{ of rows}} f(i, y) \right\} \right)^2 \quad (7)$$

A nonlinear contrast stretching is then performed on the product image ( $f(x, y) \cdot ASE(x, y)$ ) shown in Fig. 5(b) over a default piecewise value of the midpoint. The transformation is quantified as follows:

$$\mu(x, y) = \begin{cases} 2[f(x, y) \cdot ASE(x, y)]^2 & 0 \leq ASE(x, y) \leq 0.5 \\ 1 - 2[1 - f(x, y) \cdot ASE(x, y)]^2 & 0.5 < ASE(x, y) \leq 1 \end{cases} \quad (8)$$

The mean intensity for each blob  $B_n$  is computed as follows:

$$MI(B_n) = \frac{1}{Area(B_n)} \sum_{(p,q) \in B_n} \mu(p, q) \quad (9)$$

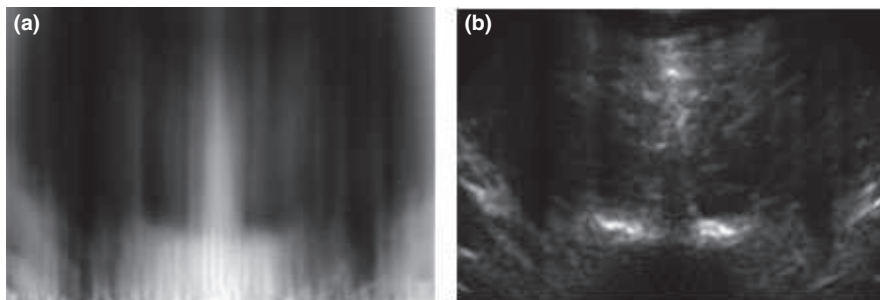


FIG. 5. (a) The ASE image. (b) The product between the ASE image and the US image.

### 2.C.2. Sum of squared residuals of the shadow region row means (SRRM) signal

In order to differentiate the spine blobs from the nonspine blobs, we cannot solely rely on the mean intensity of each ridge. For example, muscle can also represent elongated blobs with comparable mean intensities. For the selection of the following feature, we will use the notion of minimal penetration of the US signal through the bone as evidenced by the acoustic shadowing present underneath the bone surface. *In vivo* spinal US images usually do not have a completely dark region to signify acoustic shadowing but normally have a nonzero signal immediately following the spine surface. We quantify this region using the signal formed by progression of row means in the supposed shadow region beneath each blob. The scope of this region starts from the sectoral row containing the intensity-weighted centroid to the bottom oriented toward the blob's medial axis as seen in Fig. 6.

The upper side of the region is measured between scanlines containing the two extremes of the blob. Bresenham's line algorithm<sup>35</sup> is used to fit a straight-line pixel approximation to the sides of the region. For images obtained from a linear array transducer, these regions become rectangular with the last row being the bottom side. The SRRM is given by the mean intensity of each row constrained within the width of the region. The local maxima in the signal represent the presence of a high-intensity, high gradient anatomical structure like bone or connective tissue. The SRRM should ideally be a monotonically decreasing function.

An exponential decay function is modeled to fit the SRRM. The optimal fit for the exponential decay function is obtained by minimizing parameters  $\alpha_n$  and  $\beta_n$  for each blob  $B_n$  using the Levenberg–Marquardt algorithm:

$$SSR(B_n, \alpha_n, \beta_n) = \min_{\alpha_n, \beta_n} \sum_{i=1}^N (y_i - \alpha_n \cdot \exp(-\beta_n x_i))^2 \quad (10)$$

where  $y$  denotes the SRRM signal with size  $N$  and  $x$  is the depth in pixels from the intensity-weighted centroid of each blob. The minimized sum of squared residuals ( $SSR$ ) for each blob will be populated in the feature space for spine surface classification. Large residual errors from the exponential fit function would indicate, at the very least, the occurrence of a high local maximum in the signal. From

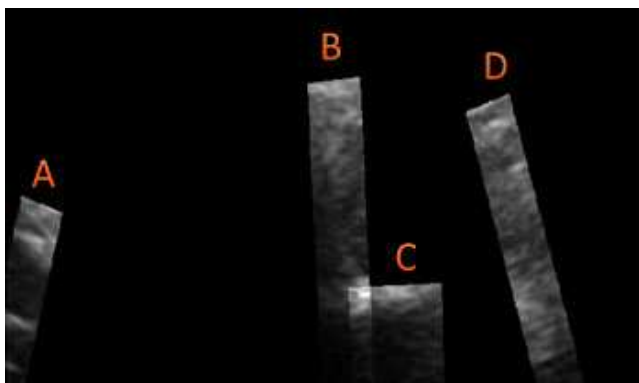


FIG. 6. The shadow region for four blobs out of 14 is shown here. B, C are spine blobs and A, D are nonspine blobs. [Color figure can be viewed at [wileyonlinelibrary.com](http://wileyonlinelibrary.com)]

Fig. 7, we observe that the SSRM values from the exponential fit function for blobs B and C (spine blobs) are relatively small in comparison to blobs A and D (nonspine blobs), where the SSRM is increased due to the presence of high local maxima. Therefore, a lower sum of these residual errors would lead to a higher likelihood of the blob corresponding to a spine surface region.

## 2.D. Classification of spine blobs

In the classification step, we aim to classify each blob in the binarized PSRE image into being either a spine blob or a

nonspine blob. Each blob described by the two features is a data point populated in the feature space. For every binarized PSRE image given as an input to the algorithm, a test set vector in  $\mathbb{R}^{n \times 2}$  is generated for the  $n$  blobs in the binarized PSRE image. A 3-nearest neighbor classification rule (3NN) is chosen to determine the points in the testing set as being a spine or nonspine blob. This is achieved by first storing all the training examples  $\langle X_{(i)}, Y_{(i)} \rangle$  and labeling them to be  $g(X_{(i)}, Y_{(i)}) = 1$  when the data point is a spine blob or 0 otherwise. When a test point  $\langle X_{(t)}, Y_{(t)} \rangle$  is encountered, the blob can be classified as spine when the majority label among the three closest training examples is 1 and nonspine otherwise. The Euclidean distance metric is used to measure “closeness.” An advantage to using the 3NN rule is that any complex decision boundary can be learned, which makes it more adaptable to noisy data. The 3NN classification shown in Fig. 8 clearly demarcates the spine blobs (green points).

In Fig. 9, we show the image before classification [Fig. 9(a)] and a binary image with just the spine blobs resulting from the application of the 3NN classification [Fig. 9(b)]. Note that only the spine blobs are retained after the classification.

## 2.E. Spine surface segmentation

According to Ref. [36], the actual bone line profile has an equi-probable likelihood of lying in between the point of highest gradient and highest intensity within the spine blob

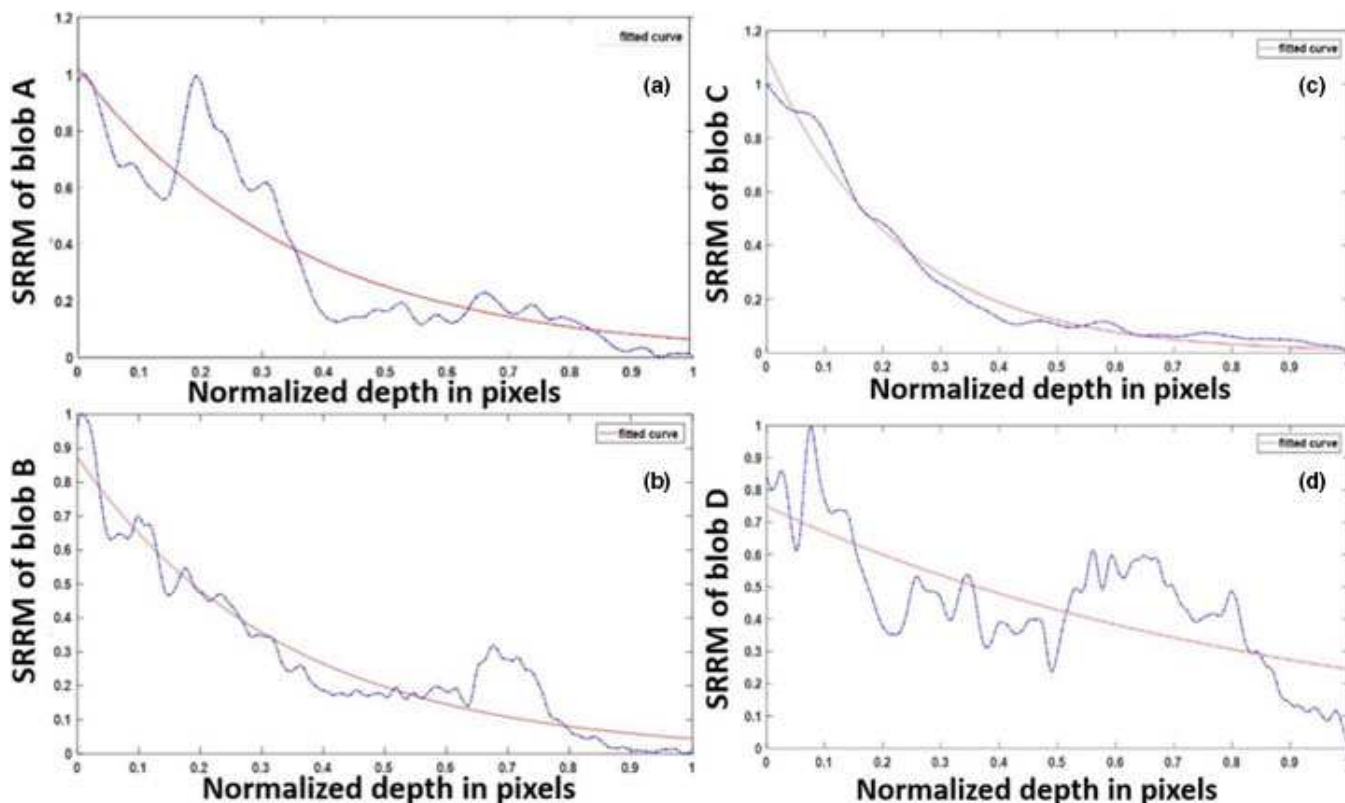


FIG. 7. The SSRM from the center of the blob (depth = 0) to the bottom of the US image (depth = 1) for the blobs A, B, C, and D shown in Fig. 7. [Color figure can be viewed at [wileyonlinelibrary.com](http://wileyonlinelibrary.com)]



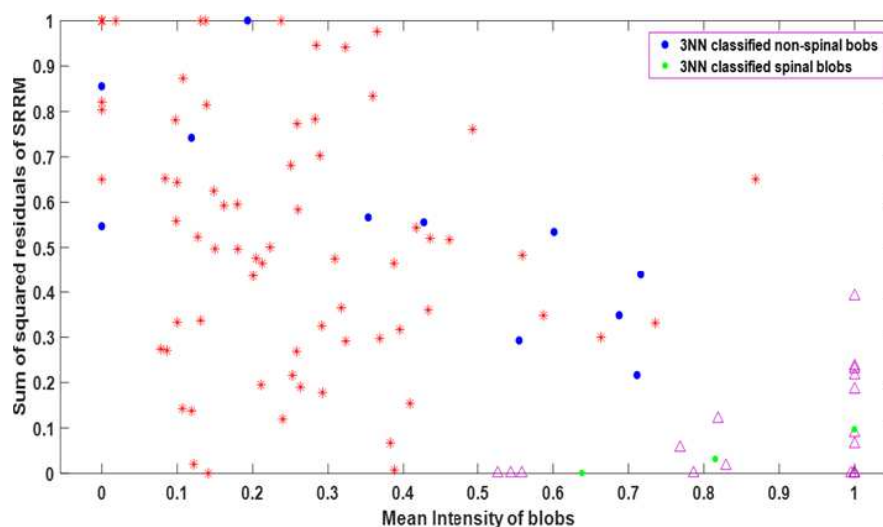


FIG. 8. Spine blob classification into spine and nonspine blobs (dots) with the training examples for spine blobs (triangles) and nonspine blobs (stars). [Color figure can be viewed at [wileyonlinelibrary.com](http://wileyonlinelibrary.com)]

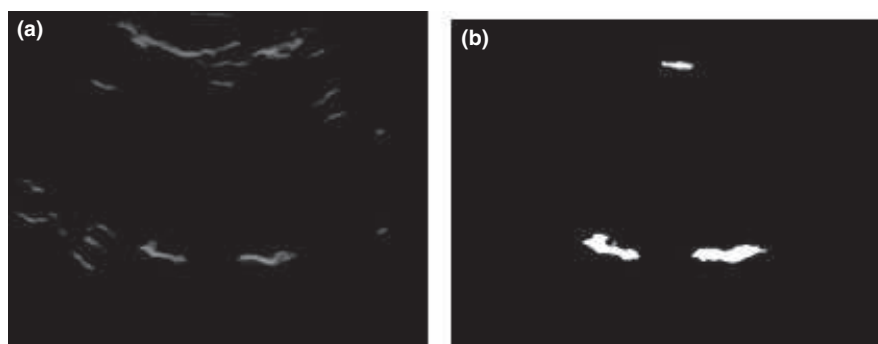


FIG. 9. (a) Product of the PSRE image and the binary image after morphological opening and (b) spine blobs retained after the spinal surface recognition step.

region. Each pixel in the line profile is the midpoint between the medial axis and the top boundary point of the spine blob for the respective scanline. Boundary points are obtained by the internal gradient. The medial axis line profile is obtained by applying the morphological skeleton to the spine blob and tracing the geodesic path between the blob endpoints to avoid spurious branches. An isotropic dilation using the distance transform is then applied to interpolate midpoint pixels between adjoining columns. The resulting spine surface segmentation is shown in Fig. 10 superimposed on the US image.

## 2.F. Experimental validation

*In vivo* B-mode images were acquired from the lumbar and thoracic regions of 17 healthy human subjects with BMI ranging from 19.5 (normal) to 27.9 (overweight). Data were acquired using a Sonix RP diagnostic ultrasound system (Analogic Medical Corp., Richmond, BC, Canada) that uses a convex array transducer with bandwidth between 2 and 5 MHz. For the reported results, all acquisitions were obtained with the center frequency set to either 3.3 MHz or 5 MHz.

The US scans were performed by first seating the subject in an upright position, and then, either the transverse or paramedian plane approach was taken. The transverse scan is more advantageous in that it enables a more comprehensive 2D visualization of a vertebral slice showing the laminae, spinous process, articular process, transverse process, LF, and the interspaces in between. For the paramedian scanning approach, the articular processes, laminae, and the interspaces spread across three vertebrae.

## 2.G. Statistical evaluation

A set of 108 US B-mode images (size:  $349 \times 603$  pixels; depth: 70 mm) were randomly selected from 30 cine loops to perform statistical evaluation of the spine surface detection. An experienced radiologist manually marked the spine and nonspine blobs in the binarized PSRE images corresponding to the visible portions of the vertebra in the B-mode images. These regions are dorsal to the vertebral foramen in spinal US and include spinous process, laminae, articular processes, and transverse processes. The blobs from each resulting binarized PSRE image were used as the test set for classification.



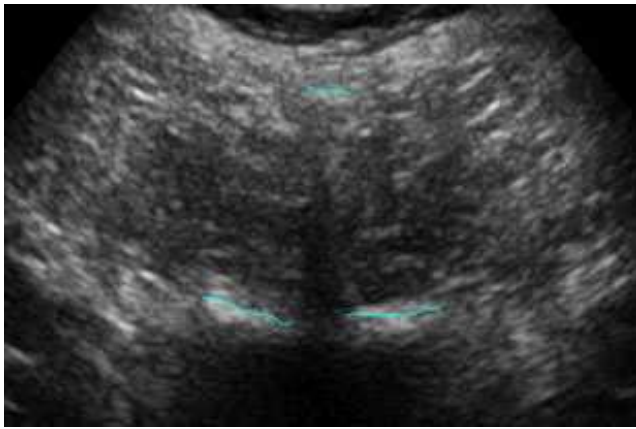


FIG. 10. Spine surface automatic segmentation given by the line profile overlaid on the original US image. [Color figure can be viewed at wileyonlinelibrary.com]

For the training set in the spine blob classification, we obtained US B-mode images from scanning the tibia bone of two sheep, radial bone of one healthy individual, and the thoracic and lumbar vertebrae of two healthy individuals *in vivo*. The different types of bones were chosen to encapsulate bone surfaces of various intensity profiles and various shadow regions and histograms. These images were first enhanced by the PSRE algorithm, and the blobs from the binary image were manually marked as bone or nonbone by the radiologist. The training examples were composed of 91 randomly selected blobs from 70 PSRE images. For evaluating the accuracy of the spine surface segmentation, the radiologist manually delineated the surface of the laminae on the US B-mode images.

### 3. RESULTS

#### 3.A. *In vivo* results

Figure 11 shows examples of spine surface automatic segmentation superimposed on a paramedian plane US image (top) and a transverse plane US image (bottom) obtained from a human subject *in vivo*. The paramedian plane US image shows the segmented laminae from lumbar vertebral levels L4, L5 and the Sacrum. The transverse plane US image from the L1–L2 intervertebral level shows the segmented articular processes, transverse processes, and the LF. Note also that the skin to LF depth can be clearly visualized in the bottom portion of the transverse image.

Figure 12 shows the qualitative performance of the proposed algorithm in three different US images across the lumbar and thoracic spines of three human subjects *in vivo*. Figure 13 shows the lumbar spines of two human subjects *in vivo* with the detected LF (highlighted in green).

#### 3.B. Statistical evaluation results

As previously mentioned, an experienced radiologist manually marked the spine and nonspine blobs in the binarized

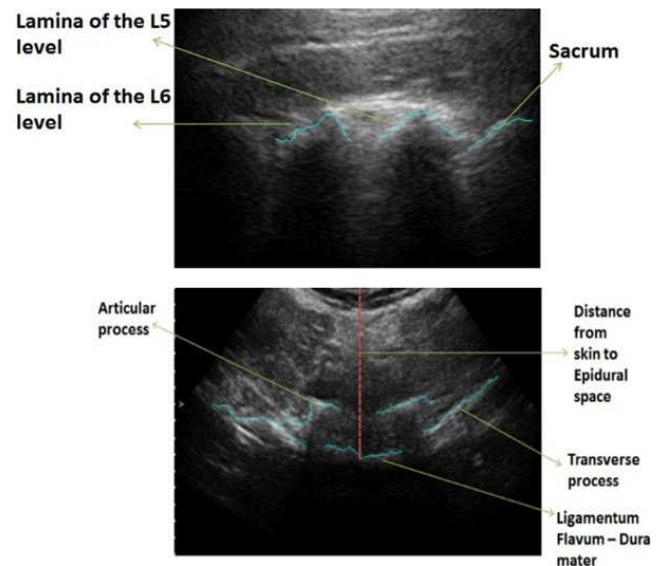


FIG. 11. Spine surface automatic segmentation on a 2D US image slice of a human subject's lumbar vertebrae *in vivo* obtained in the paramedian plane (top) and transverse plane (bottom). [Color figure can be viewed at wileyonlinelibrary.com]

PSRE images. For the purpose of illustration, Fig. 14 shows our proposed spine surface segmentation profile (magenta line) overlaid on the radiologist's manual segmentation (yellow dotted line). Note the remarkable agreement between the automatic segmentation results and the radiologist findings. We validated the spine surface detection by assessing the performance of the (a) Spine blob classification and the (b) Spine surface segmentation.

##### 3.B.1. Performance analysis of the spine blob classification

The discrimination power of the 3NN classifier in classifying spine blobs is assessed using the Geometric mean (G-mean) and Matthews Correlation Coefficient (MCC) performance measures derived from the confusion matrix given in Table I.

These measures, defined below, are chosen based on their immunity to imbalanced class sizes:

$$MCC = \frac{T_P T_N - F_P F_N}{\sqrt{(T_P + F_N)(T_P + F_P)(T_N + F_P)(T_N + F_N)}} \quad (11)$$

$$G - mean = \sqrt{\left(\frac{T_P}{T_P + F_N}\right) \left(\frac{T_N}{T_N + F_P}\right)} \quad (12)$$

The MCC value ranges from  $-1$  (never classifies correctly) to  $+1$  (perfect classification) and the G-mean values range from 0 to 1 (perfect classification). An MCC value of 0 indicates random classification. The proposed algorithm achieves an MCC of 0.77 and a geometric mean of 0.96.

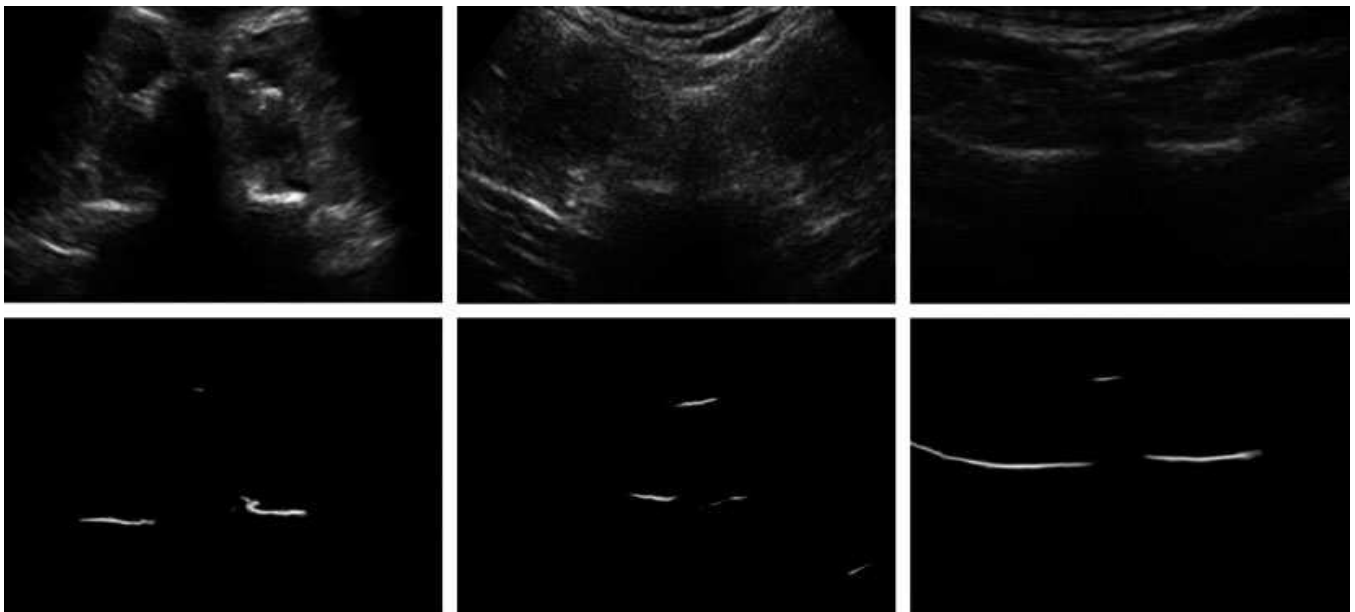


FIG. 12. Three original US images of human subjects *in vivo* obtained in the transverse plan (top) and the corresponding images after detection of spine surface regions (bottom). First column shows lumbar spine L3 level from human subject with BMI = 24.1. Second column shows lumbar spine L1 level from human subject of BMI = 27.5. Third column shows thoracic spine T5 level from human subject with BMI = 22.3.

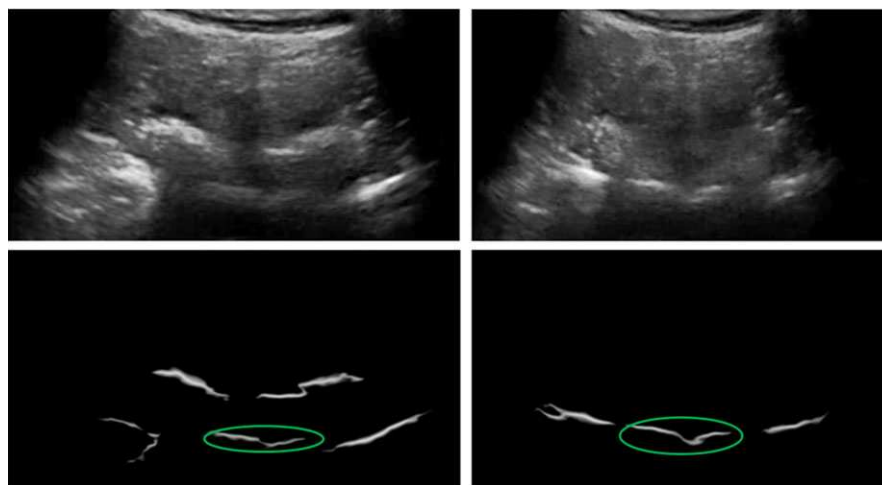


FIG. 13. Two original US images of human subjects *in vivo* obtained in the transverse plan (top) and the corresponding images after detection of spine surface regions (bottom). First column shows lumbar spine L1–L2 interspace level from human subject with BMI = 24.1. Second column shows lumbar spine L2–L3 interspace level with the LF circled. [Color figure can be viewed at [wileyonlinelibrary.com](http://wileyonlinelibrary.com)]

### 3.B.2. Performance analysis of the spine surface segmentation

The line profiles from the automatic segmentation corresponding to the laminae are evaluated against the radiologist's manual delineation of the laminae surfaces. The error metric used for our performance analysis is the mean absolute error, which is given by the following:

$$MAE = \frac{PH}{NS} \sum_{c=1}^{NS} |A(c) - M(c)| \quad (13)$$

where NS is the length of the lamina line profile in scanlines, PH is the pixel height in mm, A and M are the automatic and manual segmentation row value, respectively. The MAE (as shown in Fig. 15) is computed between the intersecting pixels of both the manual and automatic segmentations with respect to each scanline. The mean value of the mean absolute errors is 0.26 mm, and the 90th percentile of mean absolute errors is 0.44 mm with a maximum possible absolute error of 2.01 mm. This is comparable to the mean absolute errors as reported in long bones by Berton et al.<sup>31</sup> [0.38 mm between centroids of the spinous process] and Hacıhaliloglu et al.<sup>29</sup> [0.31 mm], Kowal et al.<sup>14</sup> [0.42 mm for cadavers], Foroughi

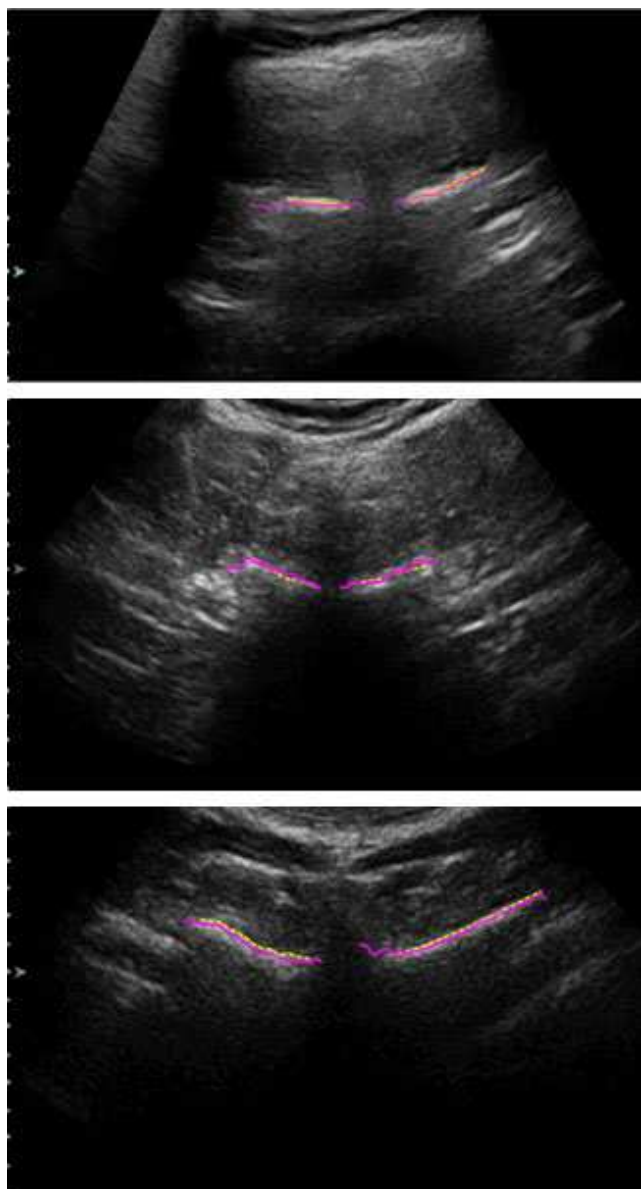


FIG. 14. Radiologist's manual segmentation of the laminae line profiles (dotted line) overlaid on the automatic segmentation (solid line). [Color figure can be viewed at [wileyonlinelibrary.com](http://wileyonlinelibrary.com)]

et al.<sup>16</sup> [0.3 mm for cadavers], Daanen et al.<sup>13</sup> [0.45 mm for patients and 0.27 mm for cadavers], and Jia et al.<sup>17</sup> [0.2 mm].

Figure 16 shows the percentage of automatic segmentation (in length) with respect to the expert segmented lamina length. From this graph, we note that the number of false positives far exceeds the number of false negatives. This is also visible from the false-positive and false-negative rate box-plots shown in Fig. 17. These rates correspond to the nonintersecting pixels of the automatic and manual segmentations. The mean false-positive rate, which computes the proportion of incorrectly identified spine pixels, is  $4.65 \pm 4.94\%$ . We encountered false-negative pixels in 6 US B-mode images with a maximum false-negative rate of 7.14%.

In terms of computational costs, the mean runtime of the algorithm was found to be equal to 7.3 s, when the algorithm

TABLE I. Confusion matrix for evaluating MCC and G-mean measures.

Class Predicted values	Actual values	
	Spine blobs	Nonspine blobs
Spine blobs	$T_P = 282$	$F_P = 151$
Nonspine blobs	$F_N = 9$	$T_N = 2548$

is run on MATLAB (Mathworks, Natick, MA, USA) in an Intel Core i3 2.3 GHz CPU with 4GB RAM. We observed a 16% decrease in runtime for images obtained from a linear array transducer.

#### 4. DISCUSSION

We have presented a new method to detect spine surfaces in US images. This method was tested on human subjects *in vivo* and validated against the manual measurements of an expert radiologist. A statistical analysis of the proposed method suggests its potentials as a new noninvasive tool to automatically detect spine surfaces in US images both for the transverse and the paramedian approaches. While the performance of our spine surface detection method was found to be statistically comparable to some of the proposed methods for long bones, to our knowledge, no other spine surface detection algorithm with comparable performance is retrievable in the literature. It should be noted that highly accurate detection of spine surfaces in US images is, in general, a very challenging task due to the geometry of the spine and the presence of multiple artifacts in the US images.

Our proposed technique relies on the robustness of the PSRE algorithm in detecting low-level features like ridges in constrained areas of the B-mode image. The PSRE algorithm depends on orientations extracted from the Radon transform for detection of line features that describe the bone surface. These orientations are used to produce ridge strength images from which the three optimal orientations and scales are obtained. The Log-Gabor filters that use these parameters are, in turn, aggregated in the phase-symmetry equation. For each blob obtained as a result, we calculate the mean pixel intensity feature from the fuzzy contrast enhanced image. The sum of squared residuals of the SRRM signal feature provides a measure for the magnitude of posterior acoustic shadowing underneath each blob. The classified blobs are segmented in concordance with the most probable location of the bone surface. Our proposed technique successfully captures line profiles of the laminae, LF, spinous, transverse, and articular processes.

A lot of the existing literatures on bone surface segmentation employ cadaveric specimens and phantoms for experiments where the acoustic shadowing area has predominantly zero intensity. Our proposed algorithm should work for any perceivable shadowing. Since the scale and orientation parameter estimation stems from the line feature detection using the Radon transform, elongated bone regions can also be detected. The use of multiple orientations for the Log-

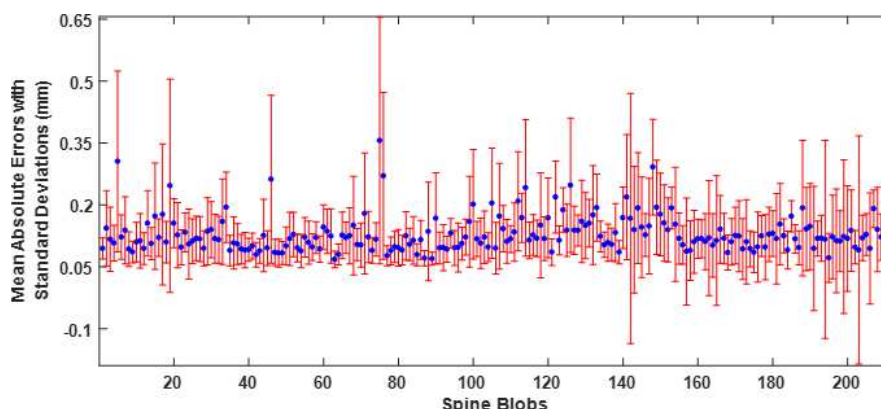


FIG. 15. Mean absolute error between the automatic and manual segmentation for the 216 laminae surfaces. [Color figure can be viewed at [wileyonlinelibrary.com](http://wileyonlinelibrary.com)]

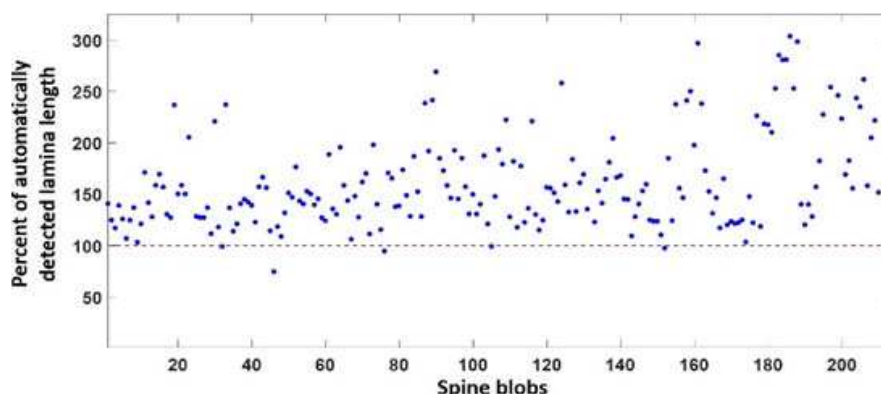


FIG. 16. Percent of the detected lamina length value (defined as automatically identified lamina length/expert segmented lamina length) for the 216 laminae surfaces. [Color figure can be viewed at [wileyonlinelibrary.com](http://wileyonlinelibrary.com)]

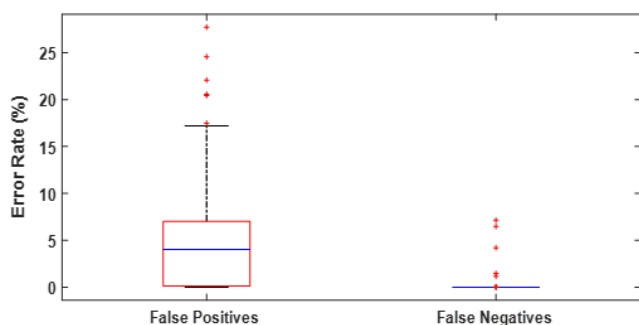


FIG. 17. The false-positive and false-negative rate boxplots for the automatic spine surface segmentation. [Color figure can be viewed at [wileyonlinelibrary.com](http://wileyonlinelibrary.com)]

Gabor filter accounts for any existing curvature of these bone regions. Filtering for optimal orientations enables spine detection even when the transducer is not aligned with the midline in the transverse view as seen in Fig. 14.

In its present form, the proposed spine surface detection method has some limitations that should be addressed in the future. The acquisition using the curvilinear transducer limits the view to relatively perceivable hyperechoic line profiles corresponding to the top surfaces of the laminae, spinous

process, articular process, and transverse process. This is due to a viewpoint obtained only at a  $90^\circ$  angle of insonication. So, the vertebral surfaces that lie nearly parallel to the direction of propagation of the ultrasonic beam cannot be interpreted and thereby delineated clearly. This results in large intensity discontinuities in the hyperechoic line profile. In the absence of fractures or abnormalities, this line profile should extend continuously along the vertebra, but it is not picked up by the PSRE algorithm. For example, Fig. 10 shows a large acoustic shadow masking most of the spinous process's surface with the exception of the upper surface that has been automatically segmented. Without knowledge of the entire surface of the spinous process, catheter placement could be misguided during the epidural or spinal. Note, however, that this is a cause for concern only when the transducer is placed above the spinous process as opposed to the interspinous space where epidural administration occurs. In the future, this issue could be curbed by acquiring multiple spinal US images in the transverse plane at oblique angles of insonication in addition to the US image obtained at  $90^\circ$ . These images can then be spatially compounded to obtain a more contiguous hyperechoic line profile that represents the entire spine surface dorsal to the vertebral foramen. In addition, statistical



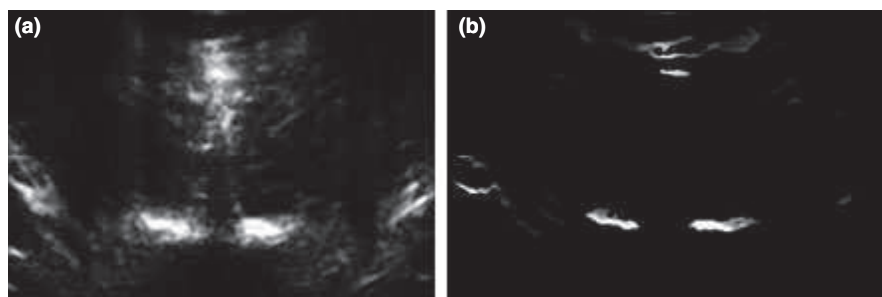


FIG. 18. (a) The fuzzy contrast enhanced image. (b) Result after multiplication with the binarized PSRE image.

shape priors as proposed in Refs. [25–27] from other modalities could be incorporated during the epidural to enforce vertebral boundary constraints. The extent of some vertebral regions, the spinous process in particular, can be crudely estimated by detecting its acoustic shadow formed underneath as explained in Ref. [31].

The false-positive rate errors in the spine surface segmentation may be attributed to limited elevational resolution. For example, the PSRE algorithm may pick up a ridge corresponding to the inferior articular process that is not present in the actual slice being imaged due to the intensity invariance of the PSRE algorithm. However, the radiologist may not perceive this because the region is construed as being less hyperechoic than the preceding or succeeding slices. This problem may be exacerbated when imaging more closely packed thoracic vertebrae, where more than one vertebra can be detected by the transducer in a given plane. The slice thickness artifact may be minimized by increasing the operating frequency, acoustic power or with the use of 2D arrays. The fuzzy contrast enhanced image [shown in Fig. 18(a)] that boosts the intensity of the hyperechoic pixels could be used as the input to the PSRE algorithm so that there is little influence of the vertebral column from slices within the vicinity of the one being imaged. However, this may have the effect of enhancing hyperechoic regions corresponding to extraneous specular artifacts and connective tissue/muscle emulating the bone line profile. Note that the fuzzy contrast enhanced image could also be used to boost the low-intensity profile of the LF, which may not be appropriately captured by the PSRE algorithm. In such cases, the ASE power can also be modified (we suggest a range of 1–3) at the expense of masking vertebral regions lateral to LF.

The false positives and negatives in the spine blob classification can also arise from the fact that we are only using hyperechogenicity and acoustic shadowing to model spine blob detection. Additional features like statistical shape priors could be incorporated into the feature space. However, the fact that the algorithm does not require *a priori* shape information is a strong advantage, which makes it suitable to virtually detect any bone surface in an US image. Furthermore, by adding more features, we run the risk of overfitting the classifier by making it too complex when adapting it to different vertebral models. For a larger depth setting

covering areas beyond the LF, we are able to visualize the posterior longitudinal ligament/vertebral body (PLL) with the hypoechogenic dural sac located between the PLL and LF. For such cases, we cropped the US images beyond the LF since the sum of squared residuals of the SRRM feature in the spine blob classification is constrained to work for blobs that have acoustic shadowing in the US image and can fail when there are hyperechogenic structures below the blob. From the vertebral slice geometry, we observe that the LF and PLL are the blobs intersecting the midline in the interspinous regions. So, a midline detection approach as mentioned in Ref. [30] can be applied after the PSRE algorithm to facilitate LF segmentation without cropping the US image.

The PSRE algorithm is constrained by the empirical setting of the angular bandwidth  $\sigma_\phi$  parameter. We could resort to the data-driven approach for estimating  $\sigma_\phi$  using Kurtosis of Radon transform (see Refs. [24,33]). There are some cases where the ridge feature strength can be improved upon by adjusting  $\sigma_\phi$  to affect the sharpness or smoothness. But this would increase the computation time due to the Radon transform calculated for a large set of possible angles and would not deter the phase-based localization of the spine surface significantly. The relatively high runtime of the proposed method can be alleviated by porting the MATLAB implementation to a GPU. Amir-Khalili et al.<sup>37</sup> has shown the feasibility of near real-time bone surface extraction on a GPU using local phase features. Finally, the availability of data from a larger number of human subjects may further help improving the performance of the classifier.

## 5. CONCLUSION

This article aims to provide a fully automated spine segmentation technique for US images. The *in vivo* experimental results demonstrate that spine blobs are detected and that the spine surface is segmented with high accuracy. The intensity invariance of the PSRE algorithm results in capturing of the full extent of the laminae, LF, transverse and articular processes, and the tip of the spinous process. The ridge detection using the PSRE algorithm and subsequent 3NN classification allow spine surface segmentation in US images acquired in both the transverse and paramedian planes.

## ACKNOWLEDGMENT

This work was partially supported by funding from the Department of Defense (grant W81XWH-14-1-0600, Log #SC130156). *In vivo* data acquisition was approved by the Texas A&M University, Human Research Protection Program (IRB #2014-0461D).

<sup>a)</sup>Author to whom correspondence should be addressed. Electronic mail: righetti@ece.tamu.edu.

## REFERENCES

- Chin KJ, Perlas A, Chan V, Brown-Shreves D, Koshkin A, Vaishnav V. Ultrasound imaging facilitates spinal anesthesia in adults with difficult surface anatomic landmarks. *Surv Anesthesiology*. 2012; 56:143–144.
- Mauldin FW, Owen K, Hossack JA. Three-dimensional spinal bone imaging with medical ultrasound for epidural anesthesia guidance. *IEEE Int Ultrason Symp*. 2011;238–241.
- Carvalho JCA. Ultrasound-facilitated epidurals and spinals in obstetrics. *Anesthesiol Clin*. 2008;26:145–158.
- Tumber SS, Liu H. Epidural abscess after multiple lumbar punctures for labour epidural catheter placement. *J Biomed Res*. 2010;24: 332–335.
- Noble JA, Navab N, Becher H. Ultrasonic image analysis and image-guided interventions. *Interface Focus*. 2011;1:673–685.
- Tran D, Rohling RN. Automatic detection of lumbar anatomy in ultrasound images of human subjects. *IEEE Trans Biomed Eng*. 2010;57:2248–2256.
- Tran D, Kamani AA, Lessoway VA, Peterson C, Hor KW, Rohling RN. Preinsertion paramedian ultrasound guidance for epidural anesthesia. *Anesth Analg*. 2009;109:661–667.
- Margarido CB, Arzola C, Balki M, Carvalho JCA. Anesthesiologists' learning curves for ultrasound assessment of the lumbar spine. *Can J Anesth*. 2009;57:120–126.
- Grau T, Leipold RW, Fatehi S, Martin E, Motsch J. Real-time ultrasonic observation of combined spinal–epidural anaesthesia. *Eur J Anaesthesiol*. 2004;21:25–31.
- Karmakar MK, Li X, Ho AM-H, Kwok WH, Chui PT. Real-time ultrasound-guided paramedian epidural access: evaluation of a novel in-plane technique. *Br J Anaesth*. 2009;102:845–854.
- Arzola C, Davies S, Rofaeel A, Carvalho JC. Ultrasound using the transverse approach to the lumbar spine provides reliable landmarks for labor epidurals. *Obstet Anesth Dig*. 2007;27:201–202.
- Rasoulia A, Rohling RN, Abolmaesumi P. Probabilistic registration of an unbiased statistical shape model to ultrasound images of the spine. *SPIE Med Imaging*. 2012;8316:1–6.
- Daanen V, Tonetti J, Troccaz J. A fully automated method for the delineation of osseous interface in ultrasound images. *Med Image Comput Assist Interv*. 2004;3216:549–557.
- Kowal J, Amstutz C, Langlotz F, Talib H, Ballester MG. Automated bone contour detection in ultrasound B-mode images for minimally invasive registration in computer-assisted surgery—an in vitro evaluation. *Int J Med Robot*. 2014;3:341–348.
- Beitzel J, Ahmadi S-A, Karamalis A, Wein W, Navab N. Ultrasound bone detection using patient-specific CT prior. *Conf Proc IEEE Eng Med Biol Soc*. 2012;2012:2664–2667.
- Foroughi P, Boctor E, Swartz MJ, Taylor RH, Fichtinger G. P6D-2 ultrasound Bone Segmentation Using Dynamic Programming. 2007 IEEE Ultrasonics Symposium Proceedings; 2007.
- Jia R, Mellon SJ, Hansjee S, Monk AP, Murray DW, Noble JA. Automatic bone segmentation in ultrasound images using local phase features and dynamic programming. 2016 IEEE 13th International Symposium on Biomedical Imaging (ISBI); 2016.
- Lopez-Perez L, Lemaitre J, Alfiansyah A, Bellemare M-E. Bone surface reconstruction using localized freehand ultrasound imaging. 2008 30th Annual International Conference of the IEEE Engineering in Medicine and Biology Society; 2008;2008:2964–2967.
- Alfiansyah A, Ng KH, Lamsudin R. Deformable Model for Serial Ultrasound Images Segmentation: Application to Computer Assisted Hip Arthroplasty. IFMBE Proceedings 13th International Conference on Biomedical Engineering; 2009.
- Wen X, Salcudean SE. P6D-5 Enhancement of Bone Surface Visualization Using Ultrasound Radio-Frequency Signals; 2007 IEEE Ultrasonics Symposium Proceedings. 2007.
- Doctor A, Vondenbusch B, Kozak J. Bone segmentation applying rigid bone position and triple shadow check method based on RF data. *Acta Bioeng Biomech*. 2011;13:3–11.
- Hussain MA, Hodgson A, Abugharbieh R. Robust Bone Detection in Ultrasound Using Combined Strain Imaging and Envelope Signal Power Detection. *Med Image Comput Comput Assist Interv*. 2014;8673:356–363.
- Hacihaliloglu I, Abugharbieh R, Hodgson AJ, Rohling RN. Bone surface localization in ultrasound using image phase-based features. *Ultrasound Med Biol*. 2009;35:1475–1487.
- Hacihaliloglu I, Abugharbieh R, Hodgson A, Rohling R. Automatic data-driven parameterization for phase-based bone localization in US using Log-Gabor filters. *Adv Vis Comput*. 2009;5875:944–454.
- Khallaghi S, Abolmaesumi P, Gong RH, et al. GPU accelerated registration of a statistical shape model of the lumbar spine to 3D ultrasound images. *Medical Imaging 2011: Visualization, Image-Guided Procedures, and Modeling*; 2011.
- Behnami D, Seitel A, Rasoulia A, et al. Joint registration of ultrasound, CT and a shape pose statistical model of the lumbar spine for guiding anesthesia. *Int J Comput Assist Radiol Surg*. 2016;11:937–945.
- Rasoulia A, Rohling R, Abolmaesumi P. Lumbar spine segmentation using a statistical multi-vertebrae anatomical shape pose model. *IEEE Trans Med Imaging*. 2013;32:1890–1900.
- Nagpal S, Abolmaesumi P, Rasoulia A, et al. A multi-vertebrae CT to US registration of the lumbar spine in clinical data. *Int J Comput Assist Radiol Surg*. 2015;10:1371–1381.
- Hacihaliloglu I, Rasoulia A, Rohling RN, Abolmaesumi P. Local phase tensor features for 3-D ultrasound to statistical shape pose spine model registration. *IEEE Trans Med Imaging*. 2014;33:2167–2179.
- Yu S, Tan KK, Sng BL, Li S, Sia ATH. Automatic identification of needle insertion site in epidural anesthesia with a cascading classifier. *Ultrasound Med Biol*. 2014;40:1980–1990.
- Berton F, Cheriet F, Miron M-C, Laporte C. Segmentation of the spinous process and its acoustic shadow in vertebral ultrasound images. *Comput Biol Med*. 2016;72:201–211.
- Loizou C, Pattichis C, Christodoulou C, Istepanian R, Pantziaris M, Nicolaides A. Comparative evaluation of despeckle filtering in ultrasound imaging of the carotid artery. *IEEE Trans Ultrason Ferroelectr Freq Control*. 2005;52:1653–1669.
- Hacihaliloglu I, Abugharbieh R, Hodgson AJ, Rohling RN, Guy P. Automatic bone localization and fracture detection from volumetric ultrasound images using 3-D local phase features. *Ultrasound Med Biol*. 2012;38:128–144.
- Kovesi P. “Symmetry and Asymmetry from Local Phase”, Proc. 10th Australian Joint Conf. Artificial Intelligence; 1997.
- Bresenham JE. Algorithm for computer control of a digital plotter. *IBM Systems J*. 1965;4:25–30.
- Jain AK, Taylor RH. Understanding bone responses in B-mode ultrasound images and automatic bone surface extraction using a Bayesian probabilistic framework. *Medical Imaging 2004: Ultrasonic Imaging and Signal Processing*; 2004.
- Amir-Khalili A, Abugharbieh R, Hodgson AJ. Using graphics processing units to enable real-time bone surface extraction from volumetric medical ultrasound image data using local PHASE features. *Bone Joint J*. 2013;95:6.